Atmospheric correction algorithm for hyperspectral remote sensing of ocean color from space

Bo-Cai Gao, Marcos J. Montes, Ziauddin Ahmad, and Curtiss O. Davis

Existing atmospheric correction algorithms for multichannel remote sensing of ocean color from space were designed for retrieving water-leaving radiances in the visible over clear deep ocean areas and cannot easily be modified for retrievals over turbid coastal waters. We have developed an atmospheric correction algorithm for hyperspectral remote sensing of ocean color with the near-future Coastal Ocean Imaging Spectrometer. The algorithm uses lookup tables generated with a vector radiative transfer code. Aerosol parameters are determined by a spectrum-matching technique that uses channels located at wavelengths longer than 0.86 μm. The aerosol information is extracted back to the visible based on aerosol models during the retrieval of water-leaving radiances. Quite reasonable water-leaving radiances have been obtained when our algorithm was applied to process hyperspectral imaging data acquired with an airborne imaging spectrometer. © 2000 Optical Society of America

OCIS codes: 010.1310, 010.4450, 120.0280, 300.6550.

1. Introduction

Imaging spectrometry can have important applications in a variety of fields, including mineral explorations, vegetation studies, and coastal monitoring. Since the mid-1980's, the concepts of imaging spectrometry[1] and hyperspectral imaging have become increasingly popular. To get useful information about the Earth's surface, one must remove the atmospheric absorption and scattering effects. An operational version of the atmosphere removal algorithm (ATREM) was developed by Gao *et al.*[2] and updated by Gao and Davis[3] for retrieving land surface reflectances from airborne- and spaceborne-imaging spectrometer data. The ATREM code has been used extensively by many investigators in a number of scientific disciplines as well as by university graduate students. With the experiences gained during the development of the land version of the ATREM code, we have developed over the past two years an operational atmospheric correction algorithm for remote sensing of ocean color from hyperspectral imaging data acquired over the coastal environment. The algorithm will be used to remove the atmospheric effects from spectral imaging data over water surfaces acquired with the Coastal Ocean Imaging Spectrometer[4] (COIS) onboard the Naval EarthMap Observer (NEMO) spacecraft.[5,6] Because the data acquired with the Airborne Visible Infrared Imaging Spectrometer[7] (AVIRIS) from a NASA ER-2 aircraft at 20 km and the near-future COIS data have similar spatial and spectral resolution and signal-to-noise ratios, we used AVIRIS data to test our algorithm during development. Figure 1 shows an example of an AVIRIS spectrum acquired over the Chesapeake Bay area in August of 1997. The major atmospheric bands, such as those of water vapor centered at approximately 0.94, 1.14, 1.38, and 1.88 μm, the oxygen band at 0.76 μm, and the carbon dioxide band near 2.06 μm, are seen. An algorithm is needed to remove atmospheric absorption and scattering effects and to derive water-leaving radiances (in reflectance units) from remotely sensed hyperspectral imaging data.

2. Background

Over the past two decades, atmospheric correction algorithms for applications to case 1 waters (i.e., clear deep ocean waters) have been developed by Howard Gordon's research group at the University of Miami.[8,9] The complexity of the algorithms has been increased greatly with time; from the early single-

B.-C. Gao (gao@rsd.nrl.navy.mil), M. J. Montes, and C. O. Davis are with the Remote Sensing Division, Code 7212, Naval Research Laboratory, Washington, D.C. 20375. Z. Ahmad is with Science and Data Systems, Incorporated, 16509 Copperstrip Lane, Silver Spring, Maryland 20906.
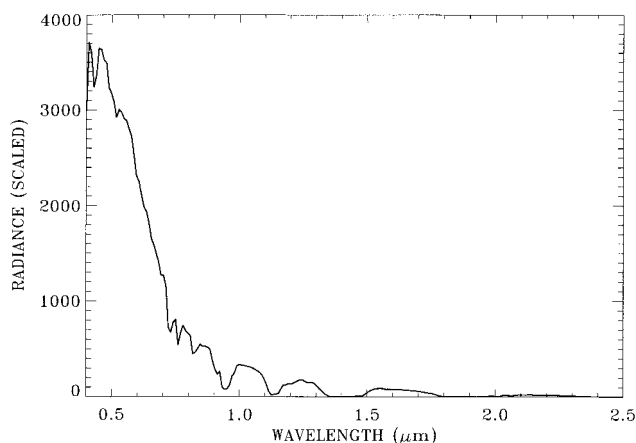
Fig. 1. Example of an AVIRIS spectrum acquired over the Chesapeake Bay area in August 1997.

scattering algorithm[8] used for the Coastal Zone Color Scanner (CZCS) to the present, more comprehensive multiple-scattering algorithm[9] for the Sea-viewing Wide Field of View Sensor (SeaWiFS). For the operational SeaWiFS algorithm, a simplified two-layer atmosphere system, i.e., aerosols confined in the bottom boundary layer and atmospheric gaseous molecules located in another layer above the aerosol layer, is assumed. An aerosol model and an aerosol optical depth are derived from channels located in the range $0.76–0.87$ μm by the assumption that water-leaving radiances are zero in the spectral range. A sophisticated lookup table procedure is used for the aerosol retrievals. The atmospheric path radiances in the visible are predicted based on the derived aerosol information. The difference between the measured radiances above the atmosphere–ocean system and the predicted path radiance is the water-leaving radiance transmitted to the top of the atmosphere.

The SeaWiFS algorithm is quite successful when it is used for processing multichannel SeaWiFS data, particularly after the radiometric calibration coefficients of SeaWiFS channels are adjusted based on theoretical simulations that use the same radiative transfer code as the one used in the generation of lookup tables. The adjustment of calibration coefficients largely removes systematic errors in both the radiative transfer code and the radiometric calibrations. However, minor defects are still present in the SeaWiFS algorithm. For example, the algorithm can produce incorrect water-leaving radiances in the visible when it is applied to pixels in the fringe of sea glint,[10] because the lookup tables used in the algorithm were generated with a radiative transfer code that assumed a flat ocean surface instead of a wind-roughened water surface.

Another operational atmospheric correction algorithm for ocean color applications has been under development for many years by Fraser *et al.*[10] This algorithm is currently implemented for processing CZCS data at a computing facility at the NASA Goddard Space Flight Center. The algorithm uses pre-

computed lookup tables generated with a vector radiative transfer code[11] that takes account of the rough ocean surface reflection, a multilayered atmosphere with mixtures of aerosols and gaseous molecules in each layer, degree of polarization of the light, and multiple scattering. The information about aerosols is derived from the 0.67-μm channel. In test retrievals, the derived water-leaving radiances in the visible channels agreed to within a few percent when both the Fraser algorithm and a version of Gordon's CZCS algorithm were applied to the same CZCS data sets acquired over clear oceanic waters without contamination by sun glint. However, the derived water-leaving radiances in the visible differed by approximately 30% when both algorithms were applied to CZCS data with weak contamination by sun glint.

For the turbid coastal environment, the water-leaving radiances in the $0.66–0.87$-μm spectral region are typically not close to zero, mainly because of scattering by suspended materials. Under these conditions, the channels in this spectral region have limited use for the retrieval of information on atmospheric aerosols. Because both the Gordon and the Fraser algorithms derive aerosol information from channels in the $0.66–0.87$-μm spectral range, these algorithms cannot easily be adapted for the retrieval of water-leaving radiances over coastal waters. In view of this situation, we have designed a different retrieving algorithm, which can use channels in longer wavelengths to derive aerosol information. A spectral matching technique is used in our retrievals.

3. Radiative Transfer

For atmospheric window channels for which the absorption by atmospheric gases is negligible, the radiance (L_{obs}) of the ocean–atmosphere system measured by a satellite instrument can be expressed as[10]

$$
\begin{aligned}
L_{obs} = {} & L_0(\lambda; \theta, \phi; \theta_0, \phi_0; \tau_a) \\
& + L_{sfc}(\lambda; \theta, \phi; \theta_0, \phi_0; W; \tau_a) t_u{}'(\lambda; \theta; \tau_a) \\
& + L_w(\lambda; \theta, \phi; \theta_0, \phi_0; W; \tau_a; O) t_u(\lambda; \theta; \tau_a), \quad (1)
\end{aligned}
$$

where L_0 is the atmosphere-scattered radiance if the radiance just above the sea surface were zero; L_{sfc} is the radiance of the light reflected from the surface, L_w is the water-leaving radiance of light scattered from beneath the surface and penetrating it, $t_u{}'$ is the upward transmittance through the atmosphere for the quantity L_{sfc}, and t_u is the upward atmospheric transmittance for the quantity L_w. L_{sfc} includes the effects of specular reflection by the air–water interfaces and the scattering effects of whitecaps. The independent parameters in Eq. (1) are defined as follows:

λ wavelength,
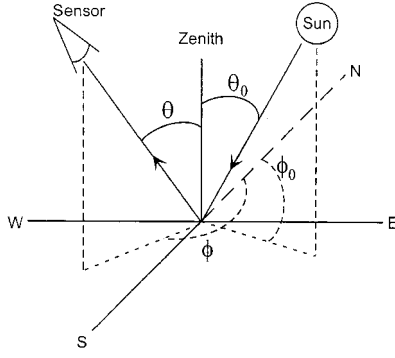θ, φ view zenith and azimuth angles from a spacecraft toward Earth's surface,

Fig. 2. Illustration for the definitions of solar zenith and azimuth angles and viewing zenith angle and azimuth angles.

θ_0, ϕ_0 Zenith and azimuth angles of the direct sunlight,

W surface wind speed,

τ_a atmospheric aerosol optical thickness,

O a parameter that represents the combined effects from all materials beneath the air–water interface.

Figure 2 illustrates the definitions of all the relevant angles. The definition of azimuth angles here follows the navigational convention. For convenience, we combine the first two terms on the right-hand side of Eq. (1) as one term, $L_{\text{atm+sfc}}$, i.e.,

$$L_{\text{atm+sfc}} = L_0(\lambda; \theta, \phi; \theta_0, \phi_0; \tau_a)$$
$$+ L_{\text{sfc}}(\lambda; \theta, \phi; \theta_0, \phi_0; W; \tau_a)t_u{}'(\lambda; \theta; \tau_a). \quad (2)$$

Substituting Eq. (2) into Eq. (1), we obtain

$$L_{\text{obs}} = L_{\text{atm+sfc}} + L_w t_u. \quad (3)$$

We follow the convention adopted in the 5S code[12] to express radiances in reflectance units. Let us denote $\cos(\theta_0)$ as μ_0 and the downward solar irradiance at the top of the atmosphere when the solar zenith angle is equal to zero as E_0. When we multiply both sides of Eq. (3) by π and divide them by $(\mu_0 E_0)$, Eq. (3) becomes

$$\pi L_{\text{obs}}/(\mu_0 E_0) = \pi L_{\text{atm+sfc}}/(\mu_0 E_0) + \pi L_w t_d t_u/(\mu_0 E_0 t_d), \quad (4)$$

where we have multiplied the numerator and the denominator of the second term on the right-hand side by the downward atmospheric transmittance t_d, which is the sum of the direct and the diffuse downward transmittances of the sunlight through the atmosphere. We use several reflectances, defined as

$$\rho_{\text{obs}}^* = \pi L_{\text{obs}}/(\mu_0 E_0), \quad (5)$$

$$\rho_{\text{atm+sfc}}^* = \pi L_{\text{atm+sfc}}/(\mu_0 E_0), \quad (6)$$

$$\rho_w = \pi L_w/(\mu_0 E_0 t_d), \quad (7)$$

where ρ_{obs}^* is the total apparent reflectance of the atmosphere–ocean system measured at the satellite level; $\rho_{\text{atm+sfc}}^*$ is the satellite level's apparent reflectance that results from the atmospheric scattering, the specular reflection, and the whitecap scattering at the air–water interface; and ρ_w is the water-leaving radiance in reflectance units, or, simply, the water-leaving reflectance. ρ_w defined here is equivalent to the quantity $[\rho_w]_N$ defined in Eq. (2) of Gordon.[13] By substituting Eqs. (5)–(7) into Eq. (4) we obtain

$$\rho_{\text{obs}}^* = \rho_{\text{atm+sfc}}^* + \rho_w t_d t_u. \quad (8)$$

To take account of the effect of atmospheric reflection of upward water-leaving radiances back to the surface, another factor, $1/(1 - s\rho_w)$, needs to be multiplied by the second term on the right-hand side of Eq. (8) [see Eqs. (11)–(13) of Fraser et al.[10]), where s is the reflectance of the atmosphere for isotropic radiance incident at its base. After this factor is inserted, Eq. (8) becomes

$$\rho_{\text{obs}}^* = \rho_{\text{atm+sfc}}^* + \rho_w t_d t_u/(1 - s\rho_w). \quad (9)$$

For hyperspectral imaging data acquired from aircraft and satellite platforms and covering the 0.4–2.5-μm spectral region, more than half of the spectral region is affected by atmospheric gaseous absorption.[2] The main contributors to gaseous absorption are atmospheric water vapor, carbon dioxide, ozone, nitrous oxide, carbon monoxide, methane, and oxygen. We denote the total atmospheric gaseous transmittance on the Sun–surface–sensor path as T_g. We further assume that the atmospheric gaseous absorption process and the molecular and aerosol scattering process can be treated independently; i.e., we neglect the interaction term between gaseous absorption and molecular and aerosol scattering. After consideration of atmospheric gaseous absorption, Eq. (9) is modified as follows:

$$\rho_{\text{obs}}^* = T_g[\rho_{\text{atm+sfc}}^* + \rho_w t_d t_u/(1 - s\rho_w)]. \quad (10)$$

Solving Eq. (10) for ρ_w yields

$$\rho_w = (\rho_{\text{obs}}^*/T_g - \rho_{\text{atm+sfc}}^*)/[t_d t_u + s(\rho_{\text{obs}}^*/T_g - \rho_{\text{atm+sfc}}^*)]. \quad (11)$$

Given a satellite measured radiance, the water-leaving reflectance can be derived according to Eqs. (5) and (11), provided that the other quantities on the right-hand side of Eq. (11) can be modeled theoretically.

4. Lookup Tables

Because of the availability of the vector radiative transfer code of Ahmad and Fraser,[11] the proper atmospheric layering structure in this code, and the treatment of wind-roughened water surfaces, we have decided to use a modified version of the Ahmad–Fraser code[11] to generate lookup tables for our retrieving algorithm. More specifically, we use the code to generate the quantities $\rho_{\text{atm+sfc}}^*$, t_d, t_u, and s in

Table 1. Relative Number Concentrations of Small and Large Particles for Four Basic Types of Aerosol Model

Aerosol Type	Percent of Small Tropospheric Particles by Number	Percent of Large Oceanic Particles by Number
1 (Maritime)	99.0	1.0
2	99.5	0.5
3	99.8	0.2
4 (Tropospheric)	100.0	0.0

Eq. (11). The code has been validated against other codes by Fraser et al.[10] The same radiative transfer code has been used by Tanre et al.[14] for remote sensing of aerosols from multichannel imaging data to be acquired with the Moderate Resolution Imaging Spectrometer (MODIS) instrument[15] onboard the Terra spacecraft. Using the code to perform radiative transfer calculations requires some input parameters, such as the vertical atmospheric temperature and pressure profiles, and aerosol models. The temperature and pressure profiles assumed are the 1976 U.S. Standard Model Atmosphere. We include no gaseous absorption in generating the quantities $\rho^*_{\text{atm+sfc}}$, t_d, t_u, and s, which are related to scattering by atmospheric molecules and aerosols.

A. Aerosol Models

The aerosol optical properties in the real coastal environment can vary significantly. To use the radiative transfer code to generate lookup tables we have to assume sets of aerosol models. Following the approach of Gordon and Wang,[9] we selected candidate aerosol models from those developed by Shettle and Fenn.[16] Most of the Shettle–Fenn models have two modes of particle size distributions—one small-particle mode (<0.1 μm) and one large-particle mode (>0.3 μm)—except for the so-called tropospheric aerosol models that have only the small-particle size mode. The smaller size fraction of the particles is a mixture of 70% water-soluble and 30% dustlike particles. The larger size fraction of the particles is made from sea-salt-based oceanic particles. The sizes of the particles in both the small size mode and the large size mode can increase as the relative humidity of the atmosphere increases. The refractive indices of the particles also change as relative humidity changes.[16] By mixing the small, tropospheric, particles with the large, oceanic, particles in different proportions, one can construct different types of aerosol model.

We have constructed four basic types of model. Table 1 lists the relative number concentrations of small and large particles for each type of aerosol model. We observed that a small change in the number of large particles in a given aerosol model can result in a significant change in the overall scattering property of the aerosol particles that correspond to the aerosol model. Gordon and Wang[9] selected the first, second, and fourth types of aerosol model. We added the third type of aerosol model to have a

smoother transition between the scattering properties of the second and the fourth types. For each type of aerosol model we selected particle sizes corresponding to five relative humidities (RH): 50%, 70%, 80%, 90%, and 98%. As a result, a total of 20 aerosol models were selected. The aerosol models that correspond to 80% RH are not included in the candidate aerosol models selected by Gordon and Wang.[9] However, these models are added to our selections based on suggestions by Eric P. Shettle of the Naval Research Laboratory. The reason behind our addition of candidate aerosol models is that the particle size changes drastically and nonlinearly at 70–90% RH, and the addition of aerosol models at 80% RH is necessary.

B. Computations

Four lookup tables for the quantities $\rho^*_{\text{atm+sfc}}$, t_d, t_u, and s in Eq. (11) have been generated. The values of $\rho^*_{\text{atm+sfc}}$ in our lookup table are computed for the 20 aerosol models described above and for the following values of independent variables:

λ 0.39, 0.41, 0.44, 0.47, 0.51, 0.55, 0.61, 0.67, 0.75, 0.865, 1.04, 1.24, 1.64, 2.25 μm;

τ_a 0, 0.1, 0.2, 0.3, 0.5, 0.7, 1.0, 1.3, 1.6, and 2.0 at 0.55 μm;

θ_0 1.5°, 12°, 24°, 36°, 48°, 54°, 60°, 66°, and 72°;

θ 0°, 1.5°, 6°, 12°, 18°, 24°, 30°, 36°, 42°, 48°, 54°, 60°, 66°, 72°, 78°, 84°, and 88.5°;

ϕ_0 0;

ϕ 0°, 12°, 24°, 36°, 48°, 60°, 72°, 84°, 90°, 96°, 108°, 120°, 132°, 144°, 156°, 168°, and 180°;

W 2, 6, and 10 m/s;

O 0;

where the τ_a values are aerosol optical depths at 0.55 μm. The grids of independent variables that we selected for computing are, in most cases, sufficient for interpolation later. In calculating the quantity $\rho^*_{\text{atm+sfc}}$ using the modified version of the Ahmad–Fraser code we assume that the water-leaving radiance at the bottom boundary is zero, and we include the effects of specular reflection at the air–water interface and the scattering by whitecaps.[10] In computing the other quantities (t_d, t_u, and s), we assume that the atmosphere is bounded by a Lambertian surface with zero reflectances at the bottom boundary.

Figure 3 shows examples of simulated 0.61-μm channel reflectance ($\rho^*_{\text{atm+sfc}}$) as a function of view angle for several relative azimuth angles. The simulations are made for a solar zenith angle of 36°, an aerosol optical depth of 0.2 at 0.55 μm, the maritime aerosol model with 80% RH, and a surface wind speed of 6 m/s. It can be seen from this figure that, for measurements within the solar plane and in the antisolar side of the half-plane ($\Delta\phi = 180$), the specular reflection from the wind-roughened water surface facets contributes significantly to $\rho^*_{\text{atm+sfc}}$ for the view zenith angles in the 60–25° range. As the relative azimuth angle decreases in the antisolar side of the
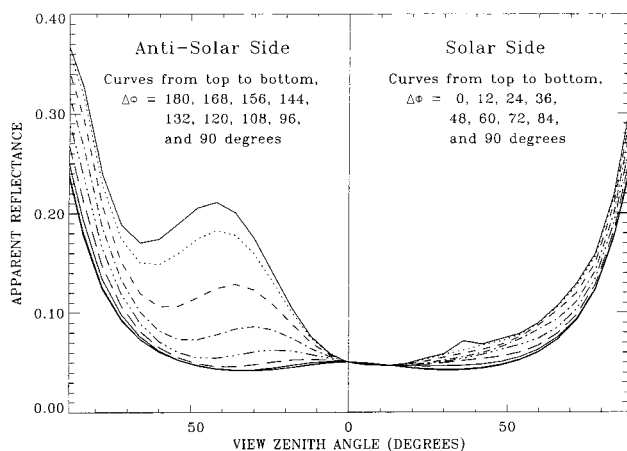
Fig. 3. Examples of simulated 0.61-μm channel reflectance ($\rho^*_{atm+sfc}$) as a function of view angle for several relative azimuth angles. The simulations are made for a solar zenith angle of 36°, an aerosol optical depth of 0.2 at 0.55 μm, the maritime aerosol model with a relative humidity of 80%, and a surface wind speed of 6 m/s.

half-plane, the specular reflection effects decrease. The specular reflection effect becomes zero for $\Delta\phi = 90°$ (i.e., when the measurements are made in the plane perpendicular to the solar plane).

Figure 4 shows examples of simulated reflectances ($\rho^*_{atm+sfc}$) as a function of wavelength for the four types of aerosol model listed in Table 1 at the same RH of 50%. The simulations are made for a solar zenith angle of 36°, a view zenith angle of 54°, a relative azimuth angle of 156°, an aerosol optical depth of 0.7 at 0.55 μm, and a surface wind speed of 6 m/s. For the first type of aerosol model (maritime aerosol model), which has the most large oceanic particles, the reflectance spectrum is flattest in the 0.4–2.25-μm spectral region. As the number of large

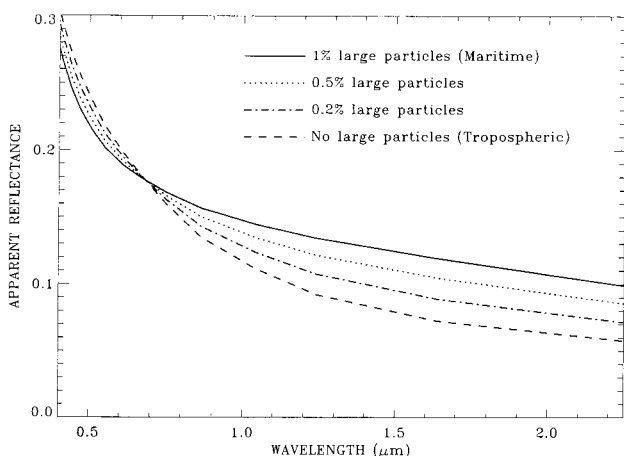Fig. 4. Examples of simulated reflectances ($\rho^*_{atm+sfc}$) as a function of wavelength for four types of aerosol model at the same relative humidity of 50%. The simulations are made for a solar zenith angle of 36°, a view zenith angle of 54°, a relative azimuth angle of 156°, an aerosol optical depth of 0.7 at 0.55 μm, and a surface wind speed of 6 m/s.

particles decreases, the reflectances decrease more rapidly with increasing wavelengths. The spectral slopes for the four curves change most rapidly in the 0.4–0.9-μm wavelength interval. This indicates that the spectra in the 0.4–0.9-μm region contain most of the information on aerosol particle sizes. The spectral slopes for the four curves also change (although less rapidly) with wavelengths in the 1.0–2.25-μm region. This indicates that the spectra in the 1.0–2.25-μm region also contain some information about particle sizes.

For the turbid coastal environment where the water-leaving radiances for channels with $\lambda < 0.9$ μm are often not close to zero, these channels are not useful for estimating particle sizes. Because the water-leaving radiances for channels above 1 μm are closer to zero for the coastal waters and because the 1.0–2.25 μm region also contains information about aerosol particle sizes, it is justified to use channels in the 1.0–2.25-μm spectral region to estimate aerosol particle sizes from remotely sensed data acquired over coastal waters. In the selection of aerosol models by Gordon and Wang, the third type of aerosol model is not included. This is equivalent to omitting the dashed–dotted curve from Fig. 4. If we concentrate on the study of spectra near 1.6 μm, we can find that the vertical intervals between the second and the fourth spectra are approximately twice as great as those between the first and the second spectra. To have a smoother transition between the scattering properties of the second and the fourth types of aerosol model, we added the third type to our candidate aerosol models.

5. Gaseous Transmittances

As shown in Fig. 1, major atmospheric absorption bands are seen in measured spectra. Typically, there are seven atmospheric gases that produce observable absorption features. These gases are water vapor (H_2O), carbon dioxide (CO_2), ozone (O_3), nitrous oxide (N_2O), carbon monoxide (CO), methane (CH_4), and oxygen (O_2).[2] A fast line-by-line-based module for calculating atmospheric gaseous transmittances was previously developed in the land version of the ATREM code.[3] In this module, high-resolution atmospheric gaseous transmittance spectra are calculated with the use of a large database ($\sim$150 Mbytes) containing precalculated high-resolution (0.05-cm^{-1}) absorption coefficients for six atmospheric gases (H_2O, CO_2, N_2O, CO, CH_4, and O_2). The database was generated by use of a line-by-line code developed by Ridgway.[17] The high-resolution spectra are smoothed to medium-resolution spectra ($\sim$0.2 nm) and merged with a medium-resolution ozone transmittance spectrum ($\sim$0.2 nm). The medium-resolution spectra are further smoothed to lower resolution to match the resolutions of instruments, such as those of the AVIRIS. This module is ported over to our ocean color version of the ATREM. Figure 5 shows an example of calculated transmission spectra at the resolution of the AVIRIS instrument ($\sim$10 nm) for a Sun–surface–sensor path and for the
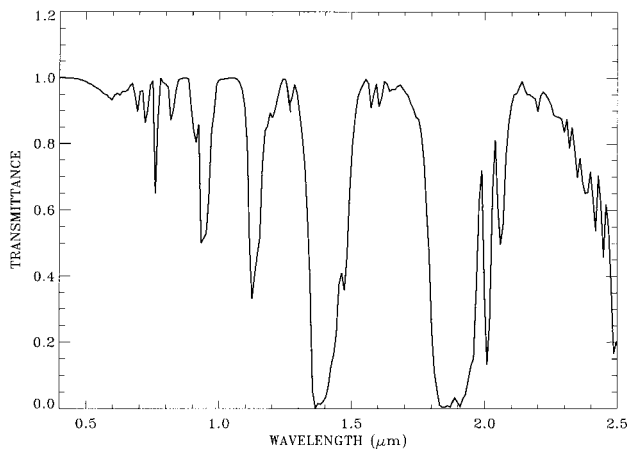
Fig. 5. Example of a calculated transmission spectrum at the resolution of the AVIRIS instrument (~10 nm) for a Sun–surface–sensor path and for seven atmospheric gases.
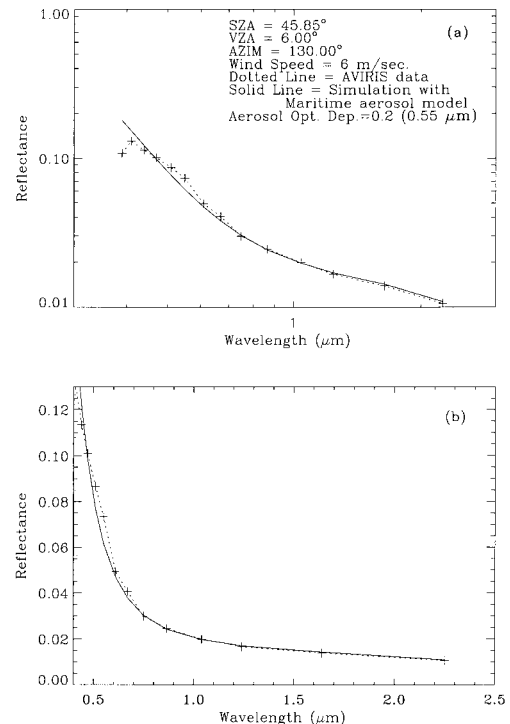

Fig. 6. (a) Examples of spectrum matching with AVIRIS data on (a) log–log plotting scales and (b) linear–linear scales. SZA, solar zenith angle; VZA, view zenith angle; AZIM, azimuth angle.

seven atmospheric gases. The major atmospheric bands, such as those seen in Fig. 1, can all be simulated with this module.

6. Retrievals

At present, the retrievals of water-leaving reflectances from measured hyperspectral imaging data cubes (two spatial dimensions and one spectral dimension) are made on a pixel-by-pixel basis. A spectral matching technique is used in the retrievals. The steps involved in the retrievals are as follows:

(a) The solar zenith and azimuth angles are derived based on the date and time of the data acquisition and on the latitude and longitude of the scene. The view zenith and azimuth angles are known.

(b) The two-way atmospheric gaseous transmittance spectra T_g, which match the spectral resolutions of all channels in an imaging spectrometer and correspond to the Sun–surface–sensor path, are calculated by the method described in Section 5. The absorption bands of atmospheric water vapor (H_2O), carbon dioxide (CO_2), ozone (O_3), nitrous oxide (N_2O), carbon monoxide (CO), methane (CH_4), and oxygen (O_2) are included in the calculations. A total of 60 transmittance spectra corresponding to vertical column water vapor amounts ranging from 0 to 15 cm are calculated. This range of column water vapor amounts covers typical atmospheric conditions in which column water vapor amounts range approximately from 0.4 to 4.3 cm. To get spectra corresponding to different water vapor amounts, we scale the water vapor vertical profile by different factors during the calculations. The transmittance spectra are stored in a lookup table.

(c) A measured radiance spectrum is divided by the solar irradiance curve[18] above the atmosphere to yield the apparent reflectance spectrum [see Eq. (5)].

(d) A water vapor amount is estimated from the 0.94- and the 1.14-μm water vapor bands in the apparent reflectance spectrum by use of a three-channel ratioing technique and a procedure to search the table containing the 60 gaseous transmittance spectra.[2] Based on the estimated water vapor value and the use of the lookup table procedure again, the best estimation of gaseous transmittance spectrum corresponding to the measured spectrum is obtained.

(e) The apparent reflectance spectrum is divided by the estimated gaseous transmittance spectrum to yield the spectrum of ρ_{obs}^*/T_g [see Eq. (11)]. The values of ρ_{obs}^*/T_g that correspond to the 14 wavelengths in our tables for scattering quantities are obtained from the spectrum of ρ_{obs}^*/T_g through linear interpolation. The 14 values of ρ_{obs}^*/T_g are used in our retrieval of an aerosol model and an optical depth by a spectrum-matching technique. Figure 6(a) shows an example of spectrum matching with AVIRIS data on log–log plotting scales. The points derived from an AVIRIS spectrum are marked with crosses and are considered to be the measured data. The dotted curve serves as a guide to the eye. In this case of spectral matching, the channels at 1.04, 1.24, 1.64, and 2.25 μm are assigned a weighting factor of 1, whereas all the other channels short of 1 μm are assigned a weighting factor of 0. The measured data for the four channels at 1.04, 1.24, 1.64, and 2.25 μm are compared with the $\rho_{atm+sfc}^*$ data stored in a precomputed lookup table for each of the 20 aerosol models and for each of the ten optical depths. The sum of squared differences between the measured data and the data in the lookup table is calculated for each of the aerosol models and for each of the aerosol optical depths. The aerosol model and optical depth

that give the smallest value of the sum of squared differences is initially selected. Another aerosol model and another optical depth that give the next-smallest value of the sum of squared differences is also selected. Using these two aerosol models and optical depths and through additional interpolating and fitting processes, we determine the final aerosol model and optical depth and the values of $\rho^*_{\mathrm{atm+sfc}}$ at the 14 wavelengths. The other scattering quantities, t_d, t_u, and s [see Eq. (11)], that correspond to the selected aerosol model and optical depth at the 14 wavelengths are determined subsequently.

The solid curve in Fig. 6(a) is the curve of $\rho^*_{\mathrm{atm+sfc}}$ versus wavelength that corresponds to our final selection of aerosol model and optical depth. The dotted curve and the solid curve agree quite well for wavelengths greater than 0.86 μm. The differences between the dotted curve and the solid curve near the 0.55-μm (green) spectral region are attributed to water-leaving radiances in the visible. For wavelengths shorter than 0.45 μm, the dotted curve is below the solid curve. This is most likely due to radiometric calibration problems of the AVIRIS instrument in the blue spectral region. Figure 6(b) is the same as Fig. 6(a), except that it is plotted on linear–linear scales.

(f) The values of the quantities $\rho^*_{\mathrm{atm+sfc}}$, t_d, t_u, and s at the wavelength grids of an imaging spectrometer are determined through interpolations and extrapolations from the corresponding values at the 14 wavelengths determined in step (e), and the water-leaving reflectance spectrum is derived according to Eq. (11).

For a hyperspectral imaging scene of approximately 30 km by 30 km with both the solar and the view zenith angles less than 55° and measured from a satellite at an altitude of 600 km or greater, the solar and view angles for every pixel in the scene can be assumed to be constants. In retrieving water-leaving reflectances from such an imaging data set, steps (a) and (b) need to be performed only once, at the beginning of the program's execution. Steps (c)–(f) are performed for each pixel spectrum.

7. Sample Results

The algorithm described in this paper was applied to derive water-leaving reflectances from a number of AVIRIS data sets. AVIRIS is an airborne imaging spectrometer[7] designed and built at the Jet Propulsion Laboratory. It simultaneously images in 224 10-nm-wide spectral bands, covering the wavelength region 0.4–2.5 μm, from a NASA ER-2 aircraft at an altitude of 20 km. The ground instantaneous field of view (one pixel) is 20 m × 20 m; the ground swath width is ~10 km. The absolute accuracy of radiometric calibration for channels from 0.45 to 2.5 μm is 5% or better. A few blue channels below 0.45 μm are less well radiometrically calibrated. The relative band-to-band accuracy in a single spectrum is a few tenths of a percent. Our retrieval results from two AVIRIS data sets, one acquired over the mouth of the
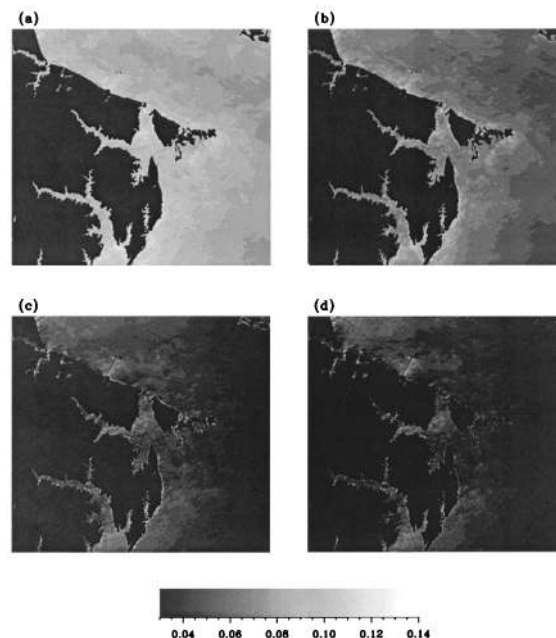

Fig. 7. AVIRIS images of (a) 0.55 μm, (b) 0.66 μm, (c) 0.865, and (d) 1.04 μm acquired over the mouth of the Chesapeake Bay (37°12′N and 76°24′W) in eastern Virginia on 17 August 1997.

Chesapeake Bay in August 1997 and another over the Florida Keys in March 1996, are described below.

A. Chesapeake Bay

The AVIRIS instrument acquired one set of spectral imaging data over the mouth of the Chesapeake Bay (37°12′N and 76°24′W) in eastern Virginia on 17 August 1997. The images of 0.55-, 0.66-, 0.865-, and 1.04-μm AVIRIS channels are shown in Figs. 7(a), 7(b), 7(c), and 7(d), respectively. The images cover the same area of approximately 11 km by 10 km. The land areas in the scene have been masked as black. The 0.66-μm image shows clearly features in the water that result from backscattering by materials suspended in the water. As the wavelength increases, the features in water are seen less clearly. This is the reason that we have used only channels at wavelengths greater than 1 μm for the derivation of aerosol information from AVIRIS data during the retrieval. Figure 8(a) shows two radiance spectra, one measured over a very turbid area (solid curve) and one over a less-turbid area (dotted line) in the AVIRIS scene. Figure 8(b) shows the water-leaving reflectance spectra retrieved from the two radiance spectra in Fig. 8(a). The overall shapes of the reflectance spectra above 0.45 μm are quite consistent with those measured from other field measurements.[19,20] Below 0.45 μm, the reflectances fall off too rapidly with decreasing wavelengths and even become negative for wavelengths less than ~0.41 μm. This problem has been observed by Carder *et al*.[21] and Hamilton *et al*.[23] for other AVIRIS scenes. It is likely due to radiometric calibration of the AVIRIS instrument, which reports too-small radiances in the blue spectral region. We do not have field-measured reflectance
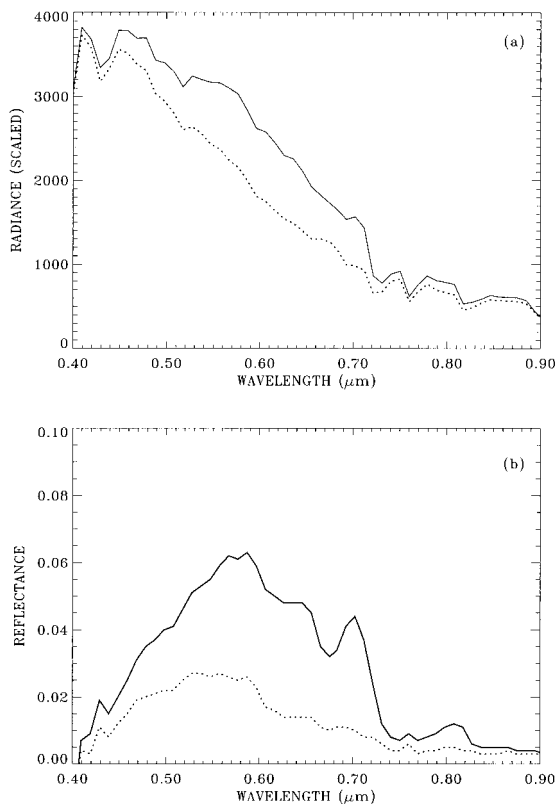
Fig. 8. (a) AVIRIS radiance spectra measured over a very turbid area (solid curve) and a less-turbid area (dotted curve) in the AVIRIS scene in Fig. 6. (b) Water-leaving reflectance spectra retrieved from the two radiance spectra in (a).

spectra corresponding to the two spectra in Fig. 8(b). Therefore it is not possible in this case study to make direct comparisons between the retrieved reflectance spectra and field-measured reflectance spectra.

B. Florida Keys

The other set of hyperspectral imaging data used in this study are the AVIRIS data acquired over the Florida Keys (24°36'N and 81°47'W) on 23 March 1996. Figure 9(a) is a color composite image of the scene. The image covers an area of approximately 50 km by 11 km. During the processing of this color image, the 0.70-μm AVIRIS channel is assigned as the red channel, the 0.55-μm channel as the green channel, and the 0.44-μm channel as the blue channel. The color image is obtained by superposition of the red, green, and blue channel images. The water is quite clear over the scene. It becomes increasingly shallow from the upper left part of the scene to the lower right part of the scene. Reflection off the bright calcium carbonate sand bottom increasingly dominates the measured spectra in the visible spectral region over shallower water areas. Figure 9(b) shows the radiance spectra extracted from the four areas marked I, II, III, and IV in Fig. 9(a). Figure 9(c) shows our retrieved water-leaving reflectance spectra. For the deepest water reflectance spectrum (marked I), the reflectance peak is centered near 0.50

μm. As the water depth decreases, the reflectance peak shifts toward longer wavelengths. For the shallowest water (marked IV), the reflectance peak is centered approximately at 0.57 μm. The shapes of the Fig. 9(c) reflectance spectra above 0.45 μm are consistent with those of field-measured reflectance spectra over similar clear waters[22] with a sand bottom in Lake Tahoe. Again, we do not have field-measured reflectance spectra that correspond to the four spectra in Fig. 9(c) for direct comparisons between the retrieved reflectances and field-measured reflectances.

8. Discussions

Although the shapes of our retrieved water-leaving reflectance spectra above 0.45 μm are consistent with those of field-measured reflectance spectra over similar waters, we do not have field-measured reflectance spectra acquired simultaneously with the AVIRIS data acquisitions. As a result, we have not been able to make direct comparisons between field-measured reflectance spectra and our retrieved surface reflectance spectra. We plan to make field measurements of reflectance spectra underneath the AVIRIS overpasses.

Our spectral matching technique and the simple weighting scheme to include or not to include a given channel in the retrieval allow us to use channels above 1 μm to derive information about atmospheric aerosols over coastal environments. By assigning a weighting factor of 1 for channels from 0.66 to 0.865 μm and a weighting factor of 0 for the rest of the 14 channels used in our lookup table, we can perform retrievals from remotely sensed data acquired over the case 1 waters for SeaWiFS or other data that do not include channels at longer wavelengths.

The scattering and absorption by molecules and aerosols occur simultaneously in the atmosphere. In this algorithm we have assumed that the atmospheric scattering process and the gaseous absorption process are two independent processes. The coupling effects between the atmospheric scattering and the gaseous absorption are not modeled. The magnitude of the coupling effects depends on the aerosol properties and surface reflectances.[23] For the dark ocean surface the coupling effects can be noticeable. For example, there is a small bump at 0.76 μm in the retrieved water-leaving reflectance spectra in Fig. 8(b). The bump is due to our overestimate of oxygen absorption near 0.76 μm when we used the two-way (Sun–surface–sensor path) atmospheric transmittance model. We can, in principle, build additional lookup tables based on rigorous radiative transfer modeling (i.e., including atmospheric scattering and gaseous absorption simultaneously during the modeling) and then develop an algorithm to remove the bump. Because a significant amount of work would be involved and it would only provide minor benefits, we have no plans at this time to develop a module for correction of the bump.

Our present lookup tables have been built for 20 aerosol models. Such lookup tables are adequate for
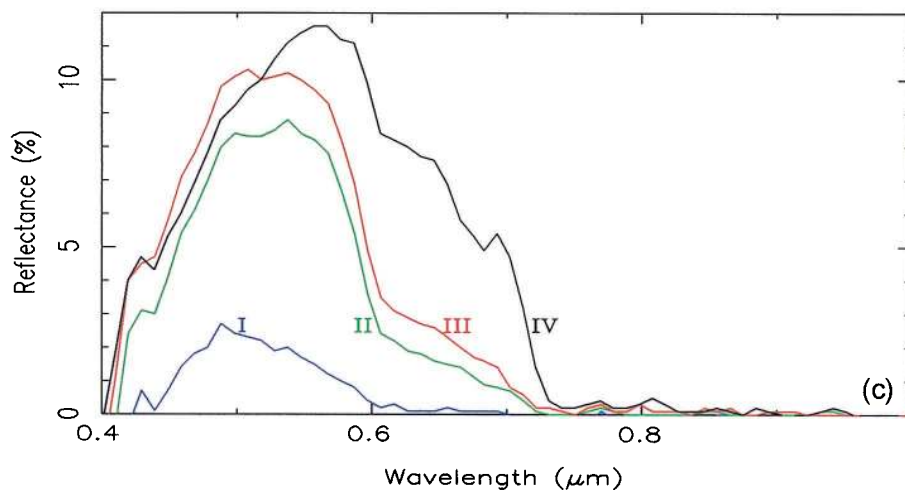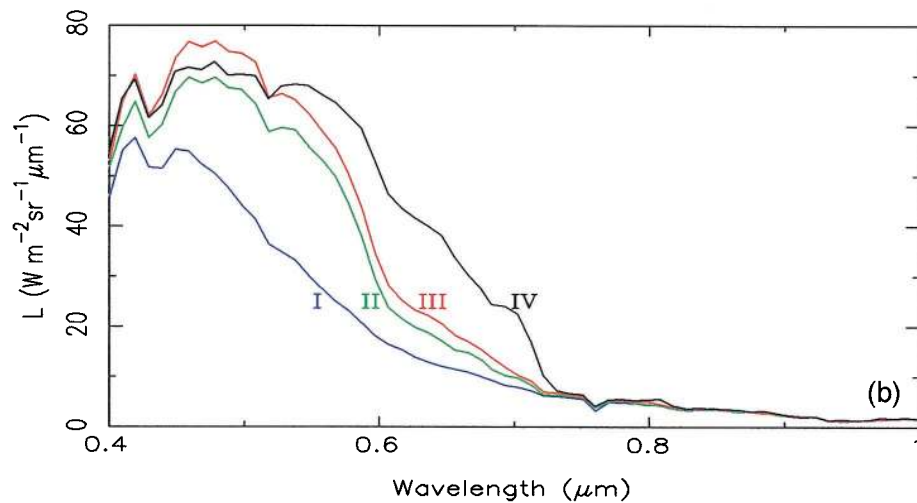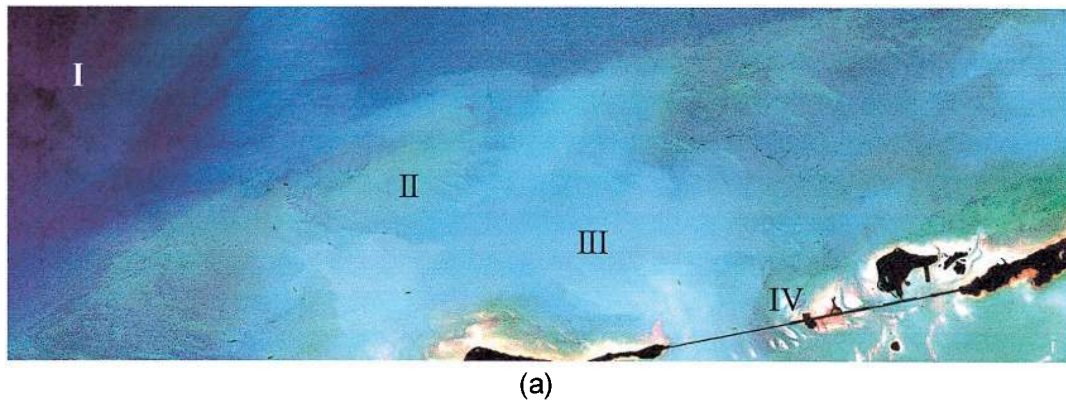
Fig. 9. (a) Color composite image of the AVIRIS scene over the Florida Keys, (b) the radiance spectra extracted from the four areas marked I–IV in (a), (c) the retrieved water-leaving reflectance spectra from the four spectra in (b). During the processing of the color image in (a), the 0.70-μm AVIRIS channel is assigned as the red channel, the 0.55-μm channel as the green channel, and the 0.44-μm channel as the blue channel. The color image is obtained by superposition of the red, green, and blue channel images.

retrievals of water-leaving reflectances from remotely sensed data acquired under typical atmospheric conditions. In the future we shall select additional candidate aerosol models, such as models for Sahara dust and Asian dust, and add simulation results with these aerosol models to our lookup tables.

We have occasionally observed from other AVIRIS data sets acquired over coastal environments that the water-leaving radiances for channels above 1 μm for

some pixels are not close to zero; such is the situation when a large amount of material is floating on the water surface. Derivation of aerosol information on aerosols from these pixels is not possible. In this situation we can use aerosol information derived from other pixels for which the water-leaving radiances above 1 μm are close to zero and extrapolate the aerosol information to these pixels when we derive water-leaving reflectances over these pixels.

9. Summary

We have developed an atmospheric correction algorithm for hyperspectral remote sensing of ocean color with the near-future Coastal Ocean Imaging Spectrometer. A spectrum-matching technique is used to derive information on atmospheric aerosols. The aerosol information is extracted back to the visible based on aerosol models during our retrieval of water-leaving reflectances. With our algorithm used to process hyperspectral imaging data acquired with the AVIRIS instrument over the Chesapeake Bay and the Florida Keys, good water-leaving reflectance spectra were retrieved.

References

1. A. F. H. Goetz, G. Vane, J. Solomon, and B. N. Rock, "Imaging spectrometry for earth remote sensing," Science **228,** 1147–1153 (1985).
2. B.-C. Gao, K. H. Heidebrecht, and A. F. H. Goetz, "Derivation of scaled surface reflectances from AVIRIS data," Remote Sens. Environ. **44,** 165–178 (1993).
3. B.-C. Gao and C. O. Davis, "Development of a line-by-line-based atmosphere removal algorithm for airborne and spaceborne imaging spectrometers," in *Imaging Spectrometry III*, M. R. Descour and S. S. Shen, eds., Proc. SPIE **3118,** 132–141 (1997).
4. C. O. Davis and K. Carder, "Requirements driven design of an imaging spectrometer system for characterization of the coastal environment," in *Imaging Spectrometry III*, M. R. Descour and S. S. Shen, eds., Proc. SPIE **3118,** 322–329 (1997).
5. T. Wilson and C. O. Davis, "Hyperspectral remote sensing technology (HRST) program and the Naval EarthMap Observer (NEMO) satellite," in *Infrared Spaceborne Remote Sensing VI*, M. Strojnik and B. F. Andresen, eds., Proc. SPIE **3437,** 2–10 (1998).
6. C. O. Davis, M. Kappus, B.-C. Gao, W. P. Bissett, and W. Snyder, "The Naval EarthMap Observer (NEMO) science and naval products," in *Infrared Spaceborne Remote Sensing VI*, M. Strojnik and B. F. Andresen, eds., Proc. SPIE **3437,** 11–19 (1998).
7. G. Vane, R. O. Green, T. G. Chrien, H. T. Enmark, E. G. Hansen, and W. M. Porter, "The Airborne Visible Infrared Imaging Spectrometer," Remote Sens. Environ. **44,** 127–143 (1993).
8. H. R. Gordon, "Removal of atmospheric effects from satellite imagery of the oceans," Appl. Opt. **17,** 1631–1636 (1978).
9. H. R. Gordon and M. Wang, "Retrieval of water leaving radiance and aerosol optical thickness over the oceans with Sea-WiFS: a preliminary algorithm," Appl. Opt. **33,** 443–452 (1994).
10. R. S. Fraser, S. Mattoo, E.-N. Yeh, and C. R. McClain, "Algorithm for atmospheric and glint corrections of satellite measurements of ocean pigment," J. Geophys. Res. **102,** 17, 107–17,118 (1997).
11. Z. Ahmad and R. S. Fraser, "An iterative radiative transfer code for ocean–atmosphere systems," J. Atmos. Sci. **39,** 656–665 (1982).
12. D. Tanre, C. Deroo, P. Duhaut, M. Herman, J. J. Morcrette, J. Perbos, and P. Y. Deschamps, "Description of a computer code to simulate the satellite signal in the solar spectrum: the 5S code," Int. J. Remote Sensing **11,** 659–668 (1990).
13. H. R. Gordon, "Atmospheric correction of ocean color imagery in the Earth Observing system era," J. Geophys. Res. **102,** 17,081–17,106 (1997).
14. D. Tanre, Y. J. Kaufman, M. Herman, and S. Mattoo, "Remote sensing of aerosol properties over oceans using the MODIS/EOS spectral radiances," J. Geophys. Res. **102,** 16,971–16,988 (1997).
15. M. D. King, Y. J. Kaufman, W. P. Menzel, and D. Tanre, "Remote sensing of cloud, aerosol and water vapor properties from the Moderate Resolution Imaging Spectrometer (MODIS)," IEEE Trans. Geosci. Remote Sens. **30,** 2–27 (1992).
16. E. P. Shettle and R. W. Fenn, "Models for the aerosols of the lower atmosphere and the effects of humidity variations on their optical properties," AFGL-TR 790214 (U.S. Air Force Geophysics Laboratory, Hanscom Air Force Base, Mass., 1979).
17. W. Ridgway, Code 913, NASA Goddard Space Flight Center, Greenbelt, Md. 20771 (personal communication, 1996).
18. H. Neckel and D. Labs, "The solar radiation between 3300 and 12500 angstrom," Solar Phys. **90,** 205–258 (1984).
19. Z. P. Lee, K. L. Carder, T. G. Peacock, C. O. Davis, and J. L. Mueller, "Method to derive ocean absorption coefficients from remote-sensing reflectance," Appl. Opt. **35,** 453–462 (1996).
20. L. Han and D. C. Rundquist, "Comparison of NIR/RED ratio and first derivative of reflectance in estimating algal-chlorophyll concentration: a case study in turbid reservoir," Remote Sens. Environ. **62,** 253–261 (1997).
21. K. L. Carder, P. Reinersman, R. F. Chen, F. Muller-Karger, C. O. Davis, and M. Hamilton, "AVIRIS calibration and application in coastal oceanic environments," Remote Sens. Environ. **44,** 205–216 (1993).
22. M. Hamilton, C. O. Davis, W. J. Rhea, S. H. Pilorz, and K. L. Carder, "Estimating chlorophyll content and bathymetry of Lake Tahoe using AVIRIS data," Remote Sens. Environ. **44,** 217–230 (1993).
23. R. S. Fraser and Y. J. Kaufman, "The relative importance of aerosol scattering and absorption in remote sensing," IEEE Trans. Geosci. Remote Sensing **GE-23,** 625–633 (1985).